The Structure and Properties of TiO₂ Nanopowders for Use in Agricultural Technologies

Tamara V. Khamova [1] , **Gennady P. Kopitsa** [1,2] , **Anton M. Nikolaev** [1,3] ,

Anastasia S. Kovalenko [1] , **Gayane G. Panova** [4] , **Olga R. Udalova** [4] , **Anna S. Zhuravleva** [4] , **Yiulia E. Gorshkova** [5] , **Vladimir P. Chelibanov** [6] , **Ivan V. Chelibanov** [6] , **Alexandr E. Baranchikov** [7] , **Natalya V. Tsvigun** [8] , **Vitaliy Pipich** [9] , **Olga A. Shilova** [1,10,*]

1   Institute of Silicate Chemistry of Russian Academy of Sciences, Saint-Petersburg, Russia
2   Konstantinov Petersburg Nuclear Physics Institute NRC KI, Orlova Roscha, Gatchina, Leningrad District, Russia
3   St.Petersburg State University, Saint Petersburg, Russia
4   Agrophysical Research Institute, Saint Petersburg, Russia
5   Frank Laboratory of Neutron Physics, Joint Institute for Nuclear Research, Dubna, Moscow district, Russia
6   OPTEC JSC, Saint-Petersburg, Russia
7   Kurnakov Institute of General and Inorganic Chemistry, Moscow, Russia
8   Federal Scientific Research Centre "Crystallography and Photonics" of the Russian Academy of Sciences, Moscow, Russia
9   Jülich Centre for Neutron Science, Forschungszentrum Jülich GmbH, Outstation at MLZ, Garching, Germany
10 St. Petersburg State Electrotechnical University "LETI", Saint-Petersburg, Russia
*   Correspondence: olgashilova@bk.ru (S.O.A.);

Scopus Author ID 6701888918

Abstract: TiO₂ nanopowder has been prepared with aqueous chemical synthesis for use in agriculture. A commercial nanopowder was taken for comparison. A comprehensive study of the phase composition, morphology, and structure of both nanopowders was carried out using methods of X-ray phase analysis, Raman spectroscopy, scanning electron microscopy, ultra-small-angle and small-angle neutron scattering, and low-temperature nitrogen adsorption. A comparison of the photocatalytic activity of these powders was carried out. Aqueous suspensions of these powders were used for the pre-sowing treatment of white cabbage seeds. A positive effect of suspensions of both titanium dioxide powders at a concentration of 0.3 g/l on the germination and biometric characteristics of plant seedlings of cabbage seedlings was revealed. As a tendency, we can note the more beneficial effect of the synthesized powder, which has a high specific surface area and porosity, is weakly crystallized in the anatase phase, and has a three-level fractal structure. No direct effect of photocatalytic activity on the germination and growth characteristics of plant seedlings was found.

Keywords: aqueous synthesis; co-precipitation; TiO₂ nanoparticle; morphology; fractal structure; biological activity; pre-sowing seed treatment

1. Introduction

Treating the crops and seeds with various compounds attracts much attention in the last decades [1-9]. Such treatment can affect metabolism, plant growth, and resistance to diseases and, therefore, bring their productivity up to a new level. Recently, the research focused on nanosized materials, e.g., oxide nanoparticles [10-18]. TiO₂ nanoparticles can be noted among other oxides because of their photocatalytic effect [19-20]. They form active forms of oxygen, hydroxyl groups, or H₂O₂ under UV-radiation. It is considered that generating the active

oxygen forms is the main mechanism of the TiO_2 toxicity, while the impact of the TiO_2 depends on the phase composition and nanoparticle size [18]. Still, opinions regarding the influence of the TiO_2 nanoparticles on crops are, to some degree, contradictory. Authors of the present paper have earlier established a positive effect of the TiO_2 nanoparticles on the germination of Chinese cabbage, on the diversity and seedlings of the epiphytic microorganisms state [21]. At the same time, the exact influence of the discrete physical characteristics of the TiO_2 on the early growth stages isn't clarified. The present work focuses on the thoughtful research of the physical characteristics of the TiO_2 nanoparticles; specifically phase composition, morphology, and photocatalytic properties compared with commercial TiO_2 powder. Also, the efficiency of the pre-sowing treatment of the white cabbage with TiO_2 powder has been evaluated.

2. Materials and Methods

2.1. Materials.

Two samples of TiO_2 powders were used in the present work. Synthetic TiO_2 powder, denoted as TiO_2 (*Syn*), was prepared as follows. 15 ml of $TiCl_4$ were added to the 300 ml of water-cooled to the 0 °C with pH value 1 (corrected with HCl). Then 150 ml of 12.5% NH_3 solution was added dropwise into it under vigorous stirring up to pH value 12. The slurry was filtered, washed with distilled water, and dried at 105 °C. Commercial powder, denoted as TiO_2(*Com*), made by Plasmotherm® company, was used as the reference.

2.2 Methods.

X-ray diffraction (XRD) and Raman spectroscopy were used for the phase analysis of the samples. X-ray Measurements were carried out using the Bruker D8 Advance diffractometer (CuK_α-radiation) in the 2θ range 10°–90° with 0.02° step and 0.3 s exposition. Raman spectra were obtained using the equipment OPTEC-785TRS-2700 of JSC OPTEC (St. Petersburg, Russia). The range of Raman frequency equals 200…2700 cm^{-1}; terahertz frequency range is −200…−10 cm^{-1} (−6.0…−0.3 THz), and 10…200 cm^{-1} (0.3…6.0 THz). The wavelength of laser radiation (single-mode) is 785 nm (bandwidth ≤100 MHz). The spectral resolution of the system is at least 3.5 cm^{-1}. Laser power (adjustable) is 0…100 mW.

The surface morphology of the powders was studied by scanning electron microscopy (SEM) using Carl Zeiss N Vision 40 equipment at 1 kV accelerating voltage and magnification up to 300 000x.

The nanopowders' texture characteristics were evaluated by the low-temperature nitrogen adsorption method using Quantachrome Nova 1200e analyzer. The samples were degassed at 150°C in the vacuum for 15 hours before the measurements. The specific surface area of the samples (S_{sp}) was calculated with the Brunauer–Emmett–Teller (BET) model by 7 points within the range of partial pressure of nitrogen P/P_0 0.07 ÷ 0.25. Langmuir model was used for the S_{sp} value evaluation in the cases of the large or negative values of the C constant [22]. The specific pore volume was measured in the range of high partial nitrogen pressures $P/P_0 \cong 0.995$. The pore size distribution was calculated by analyzing the desorption branches of the total adsorption-desorption isotherms (in the range of nitrogen partial pressure 0.01 – 0.99) using the Barrett-Joyner-Halenda (BJH) model.

Small-angle neutron scattering (SANS) and Ultra small-angle neutron scattering (USANS) measurements were carried out at the YuMO (IBR-2 reactor, Dubna, Russia) and

KWS-3 (FRM-II, Garching, Germany) facilities, respectively. The YuMO setup is a time-of-flight small-angle spectrometer [23] operating in a geometry close to a point, using two ring He^3-detectors located at sample-detector distances SD = 4 and 13 m, respectively. The flux of thermal neutrons with wavelength $\lambda = 0.05 \div 0.8$ nm was formed in the collimator system so that neutrons directed to the sample formed a beam of 14 mm in diameter with an intensity of up to 4×10^7 neutrons. The range for the momentum transfer $q = (4\pi/\lambda) \cdot \sin(\theta/2)$ (where θ is the scattering angle) was $0.06 - 5$ nm^{-1}. The experimental data were processed using the SAS program [24], allowing the obtained spectrum to be normalized to an independent vanadium scatterer and subtracting the background sample data [25].

The KWS-3 setup is a small-angle diffractometer operating with the focusing toroidal mirror, making it possible to achieve a high resolution in the momentum transfer up to $1 \cdot 10^{-3}$ nm^{-1} [26,27]. The measurements were carried out at neutron wavelength $\lambda = 1.28$ nm ($\Delta\lambda/\lambda = 0.2$) and sample-detector distance SD = 10 m, which made it possible to measure the neutron scattering intensity in the range of momentum transfer $1.3 \cdot 10^{-3} < q < 2.3 \cdot 10^{-2}$ nm^{-1}.

Scattered neutrons were registered by a two-dimensional position-sensitive scintillation detector based on ^{6}Li (the core diameter is 8.7 cm with a spatial resolution of 0.36 x 0.39 mm^2). The raw spectra were corrected using the standard procedure [27], taking into account scattering by the setup equipment and quartz glasses, as well as the background. The obtained two-dimensional isotropic spectra were azimuthally averaged and brought to absolute values by normalizing to the cross-section of incoherent Plexiglas scattering taking into account the detector efficiency [28] and the thickness L for each of the samples. For the preliminary data processed, the QtiKWS program was used [29].

To determine the photocatalytic activity of TiO$_2$ nanopowders, we estimated the amount of singlet oxygen released under ultraviolet radiation. Concerning our study, this was especially important since active oxygen forms inhibit the growth of pathogenic flora. The measurements were carried out on the equipment of JSC OPTEC (St. Petersburg, Russia). The photocatalytic activity of the synthesized powder was evaluated by the efficiency of singlet oxygen giving out compared to the standard – in our case, with the commercial TiO$_2$ (*Com*) powder manufactured by Plasmotherm®. The test setup consisted of a singlet oxygen generator, model GSK-1, and a chemiluminescent singlet oxygen gas analyzer, model 1O2 [30]. Identical weighed portions (2 mg each) of titanium dioxide powder and the reference were separately applied to porous fluoroplastic membranes, which were alternately placed in a GSK-1 generator, where they were illuminated with a CHANSON LED matrix (P = 10 W, $\lambda = 365$ nm). Air was preliminarily dried and purified from reactive oxygen species using a carbon filter. Then the air was pumped through a membrane and supplied to a singlet oxygen gas analyzer. Singlet oxygen was formed in the membrane upon the UV-activated photocatalyst interaction with ordinary triplet oxygen molecules in the pumped air [30,31]. Due to the low photocatalytic activity of the studied powders, the concentration of singlet oxygen produced by them is not given in the usual form (μg/m^3) but relative units corresponding to the photocurrent from the chemiluminescence sensor [30].

The study of the biological activity of titanium dioxide powders was to determine their effect on the germination energy and germination of seeds as well as on the growth characteristics of their seedlings. White cabbage variety Penca de Povoa (к-2558, Portugal) from the collection of N.I. Vavilov All-Russian Institute of Plant Genetic Resources (VIR) was used as the test subject. Presowing seed treatment was carried with aqueous suspensions of titanium dioxide powders in concentrations of 0.3 and 3 g/l by mixing for 10 minutes. The

seeds were then dried at room temperature in air and at 30° C for 60 minutes in an oven. Seed drying methodic corresponded to these specified in GOST 12038 (GOST 12038–84). Cabbage seeds were germinated in Petri dishes 10 cm in diameter on filter paper soaked in 10 ml of the test substance's aqueous solution.

Control seeds were germinated in distilled water. On the 3rd day, the energy of seed germination was measured. On the 7th day – their germination (GOST 12038–84), and the length of shoots and roots of seedlings was measured. The studies were carried out following the International Seed Testing Association (ISTA) rules and generally accepted methods [32]. Repetition of the experiment - 400 seeds for each variant of the experiment. All experiments were repeated three times.

3. Results and Discussion

3.1. Structure and morphology of TiO₂ nanopowders.

The results of X-ray phase analysis of the studied titanium dioxide powders are shown in Figure 1. Commercial TiO_2 (Com) is a well-crystallized titanium dioxide consisting of a mixture of anatase and rutile in a ratio of approximately 1:4, respectively, while synthesized TiO_2 (Syn) is a poorly crystallized titanium dioxide in the form of anatase.

This result correlates with Raman spectroscopy data (Figure 2). Commercial TiO_2 (*Com*) (Figure 2 (a)) has bands typical both for rutile (241, 445, 610 cv^{-1}) and anatase (weak band at 516 cm^{-1}). Anatase bands at 397 and 638 cm^{-1} are superimposed on more intense rutile bands and appear in their asymmetry. Synthetic TiO_2 (*Syn*) (Figure 2 (b)) has solid bands typical for anatase (397, 516, 638 cm^{-1}).
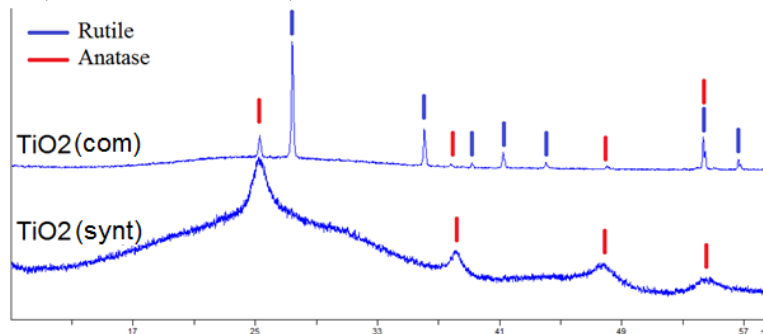

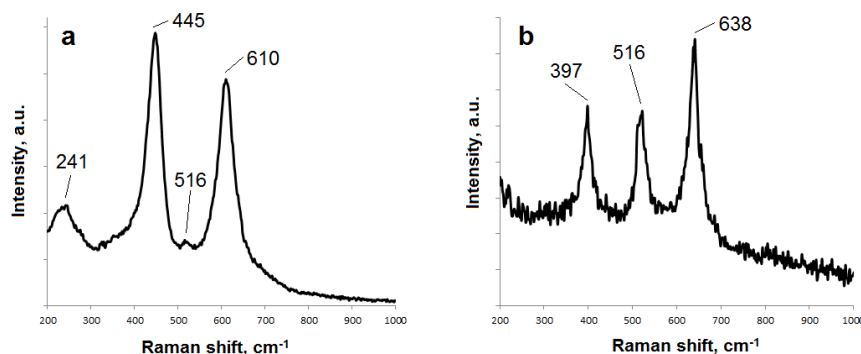**Figure 1**. X-ray diffraction patterns of the TiO_2 powders.

Figure 2. Raman spectra for the nanopowders: (**a**) commercial TiO_2 (*Com*); (**b**) synthesized TiO_2 (*Syn*).

Scanning electron microscopy (Figure 3) showed that well-crystallized commercial TiO_2 (*Com*) is a nanopowder consisting of aggregates of ~65-500 nm size, while synthesized

TiO$_2$ (*Syn*) is a nanopowder with a poorly crystallized porous structure, consisting of aggregates of ~ 50-100 nm in size.
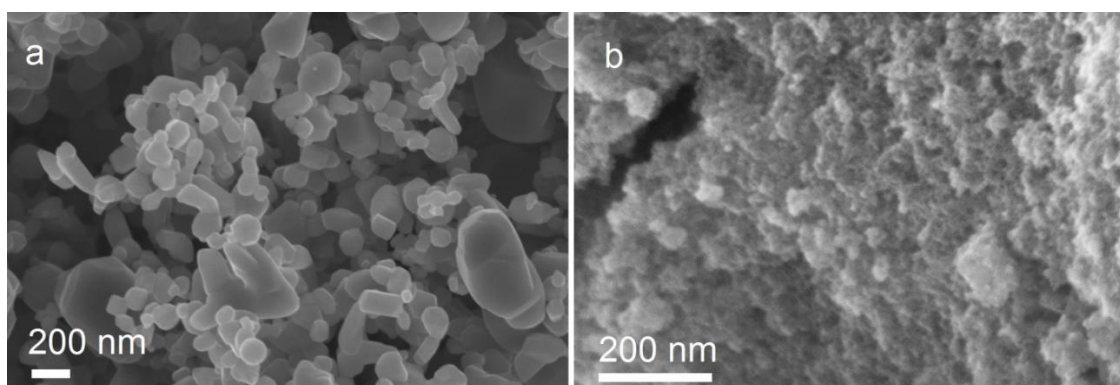
Figure 3. SEM images of powders: (**a**) commercial TiO$_2$ (Com); (**b**) synthesized TiO$_2$ (Syn).

Complete nitrogen adsorption-desorption isotherms for the TiO$_2$ powders are shown in Figure 4 (a, b). Judging by its form, the adsorption isotherm for commercial TiO$_2$ (*Com*) (Figure 4 (a)) belongs to type I according to the IUPAC classification, i.e., isotherm, which is characteristic for microporous materials. The shape of the hysteresis loop confirms it for the sample, which can be assigned to the H4 type typical for the microporous materials with slit pores. Also, the hysteresis loop closes at the values of the relative pressure P/P$_0$ significantly less than 0.3 (Figure 4 (a)), which also indicates the presence of a significant number of micropores in the TiO$_2$ (*Com*) sample.
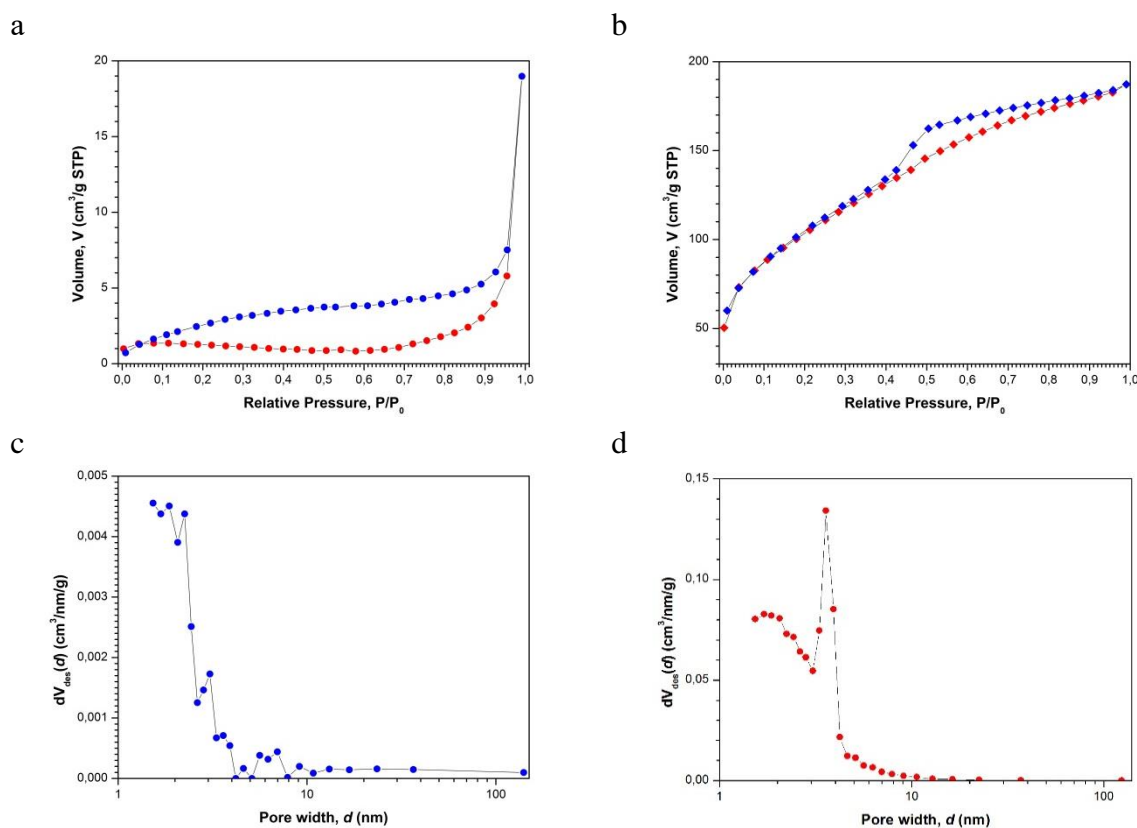
Figure 4. Complete nitrogen adsorption-desorption isotherms (**a, b**) and pore size distributions (**c, d**) plotted by processing the complete nitrogen desorption isotherms using the BJH model for TiO$_2$ powders: (**a, c**) commercial TiO$_2$ (*Com*); (**b, d**) synthesized TiO$_2$ (*Syn*).

The nitrogen adsorption-desorption isotherm of the synthesized TiO$_2$ (*Syn*) – Figure 4 (b), corresponds to type IV and is characterized by vivid capillary-condensation hysteresis of

the H2 type, which indicates the presence of cylindrical mesopores with narrow constrictions in it. The results of the analysis of the obtained isotherms using the Langmuir, Brunauer-Emmett-Teller (BET), and Barrett-Joyner-Halenda (BJH) models are presented in Table 1 and Figure 4 (c, d)

As can be seen from Table 1, commercial TiO$_2$ (*Com*) nanopowder has a small specific surface area $S_{Langmuir}$ = 5.9 ± 0.2 m^2/g. The Langmuir model can be applied only in monomolecular adsorption, i.e., adsorption on micropores' surface. It indicates a low porosity of this powder and correlates with a small specific pore volume $V_{P/P0 \to 0.99}$ = 3.1·10^{-2} cm^3/g.

TiO$_2$ (*Syn*) nanopowder synthesized by precipitation has a developed surface S_{BET} = 369 ± 7 m^2/g (determined using the Brunauer – Emmett – Teller (BET) model with 7 points in the range of partial nitrogen pressures P/P$_0$ = 0.07 ÷ 0.25) and relatively large specific pore volume $V_{P/P0 \to 0.99}$ = 2.7·10^{-1} cm^3/g.

Table 1. Texture parameters of the studied TiO$_2$ powders, calculated by analyzing the complete nitrogen adsorption-desorption isotherms using the Langmuir, BET, and BJH models.

Sample	$S_{Langmuir}$, m^2/g	S_{BET}, m^2/g	$V_{P/P0 \cong 0.995}$, cm^3/g)	d_{p1}, nm BJH (des)	d_{p2}, nm BJH (des)
Commercial TiO$_2$ (*Com*)	5.9 ± 0.2	-	0.031	-	-
Synthetic TiO$_2$ (*Syn*)	-	369 ± 7	0.270	1.7	3.6

Note/ $S_{Langmuir}$ & S_{BET} – specific surface area, $V_{P/P0 \to 0.99}$ – specific pore volume; d_{p1}, d_{p2} – average pore diameter, parameters determined from the analysis of total nitrogen adsorption-desorption isotherms using the Langmuir, BET, and BJH models, respectively.

Mathematical processing of the complete nitrogen adsorption-desorption isotherms using the BJH model made it possible to obtain pore size distribution (Figure 4 (c, d)). As can be seen from Figure 4 (c), commercial TiO$_2$ (*Com*) powder is characterized by the presence of the micropores without a definite maximum and by a rapidly decreasing pore distribution in the region d> 2.5 nm, which indicates the absence of meso and macropores in this material. At the same time, for the synthesized TiO$_2$ (*Syn*) powder (Figure 4 (d)), a bimodal pore size distribution is observed with the maximum at dp$_1$ ≈ 1.7 and dp$_2$ ≈ 3.6 nm, respectively.

To obtain complete information on the size and shape of inhomogeneities in the studied titanium dioxide powders, the SANS and USANS methods were applied, widely used to study the meso- and microstructure of various materials in the scale range from 1 nm to several microns. The experimental dependencies of d$\Sigma(q)$/dΩ of small-angle and ultra-small-angle neutron scattering vs. the momentum transfer q for the TiO$_2$ powders are presented in Figure 5. The nature of the observed SANS and USANS of TiO$_2$ samples differs depending on the degree of their crystallization.

The scattering curve for synthesized TiO$_2$ (*Syn*) can be divided into three ranges regarding the momentum transfer q, where the behavior of the scattering cross-section d$\Sigma(q)$/dΩ obeys power laws $q^{-\Delta}$ with different values of the exponents $\Delta = n_1$, n_2, and n_3, respectively (Fig. 5a). At the same time, in intermediate regions, as well as at small $q < 0.002$ nm^{-1}, the behavior of the scattering cross-section d$\Sigma(q)$/dΩ is satisfactorily described by an exponential dependence (Guinier regime).
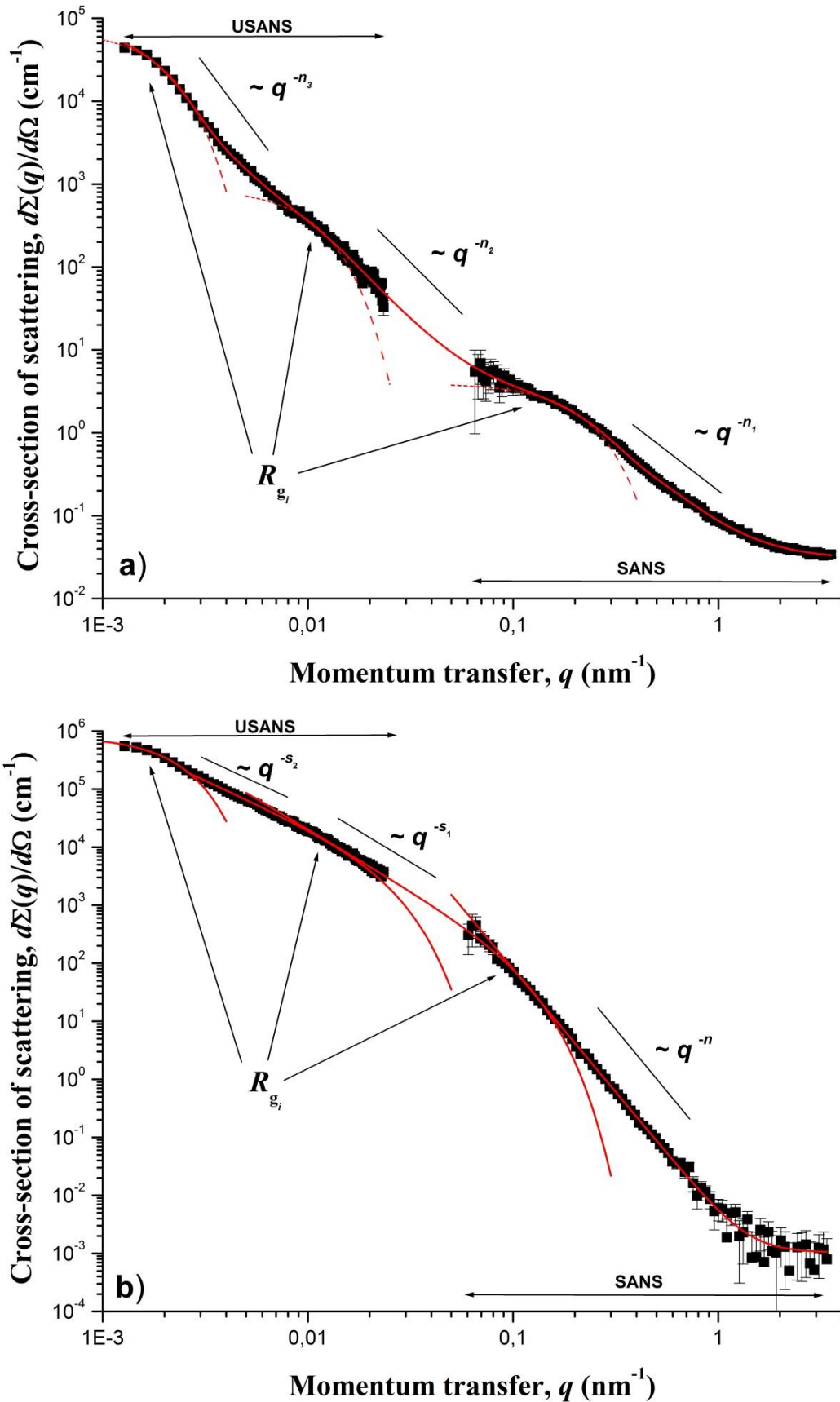
Figure 5. Dependences of the differential macroscopic cross-section $d\Sigma(q)/d\Omega$ of USANS and SANS vs the momentum transfer q for the TiO$_2$ powders: a) synthesized TiO$_2$ (*Syn*), b) commercial TiO$_2$ (*Com*). Solid lines – fit of experimental data according to formulas (1) and (4).

Thus, the scattering pattern observed for synthetic TiO$_2$ (*Syn*) is typical for scattering at the three-level hierarchical structure [33-36], with a different characteristic scale and type of aggregation for each of the levels. The scattering from the first (smaller in scale) of these structural levels observed in the region of large $q > 0.25$ nm^{-1} is described by the power-law q^{-n_1}. The value of the exponent n$_1$ found from the slope of the straight-line region of the experimental curve d$\Sigma(q)$/dΩ is $n_1 = 2.23 \pm 0.04$. It is known [37] that the values of the exponent $1 < 1 < 3$ correspond to scattering on objects with the mass-fractal aggregation of inhomogeneities (clusters) with fractal dimension $D_{m1} = n_1$.

Deviations from the q^{-n1} power law in the scattering cross-section d$\Sigma(q)$/dΩ for synthesized TiO$_2$ (*Syn*) are observed in the region of $0.09 < q < 0.25$ nm^{-1} and large momentum transfer q. At $q < 0.25$ nm^{-1}, this deviation is associated with entering the Guinier regime [38], where the scattering is determined by the characteristic size R_{c1} (in the case of fractal systems, the upper self-similarity limit) of independently scattering fractal objects. From the analysis of scattering in the Guinier regime from the slope of the curves $\ln($d$\Sigma(q)$/d$\Omega)$ versus q^2, we can obtain an estimate of the gyration radius R_{g1} of fractal objects and therefore their usual size R_{c1}, which in the case of fractal objects related by the equation $R_{c1} = \left[(D_{m1} + 2)/D_{m1}\right]^{1/2} \cdot R_{g1}$ [39]. It is worth mentioning that the value of the gyration radius R_g corresponds to the maximum of the inhomogeneities size, which contributes to the observed scattering in the Guinier regime.

In the range of large momentum transfer, the scattering cross-section d$\Sigma(q)$/dΩ doesn't depend on q (i.e., becomes a constant). It is caused by the incoherent scattering by hydrogen atoms included in the composition of a given sample is chemically bound or sorbed water. Therefore, the observed scattering analysis and the estimation of the lower bound of self-similarity of mass fractal clusters are not possible.

The scattering from the second structural level observed in the range of transmitted pulses $0.01 < q < 0.09$ nm^{-1} is described by the power-law q^{-n2} with the exponent $n_2 = 2.61 \pm 0.04$. As in the case of the first structural level, it corresponds to scattering on objects with the mass-fractal aggregation of inhomogeneities (aggregates) with fractal dimension $D_{m2} = n_2$. The lower limit of self-similarity of mass-fractal aggregates of a given structural level is determined by the characteristic size R_{c1} of mass-fractal clusters of the first structural level. An estimate of the upper limit of self-similarity of mass-fractal aggregates of the second structural level can be obtained from the analysis of scattering in the Guinier regime in the range $0.006 < q < 0.01$ nm^{-1}: $R_{c2} = \left[(D_{m2} + 2)/D_{m2}\right]^{1/2} \cdot R_{g2}$.

The scattering from the third (largest in size) structural level observed in the range of $0.002 < q < 0.006$ nm^{-1} is described by the power-law q^{-n3} with the exponent $n_3 = 3.61 \pm 0.07$. It corresponds to the scattering by inhomogeneities (agglomerates) with a highly developed fractal surface [40] of phase interface (solid-phase - pore), the dimension of which is determined as $D_{s3} = 6 - n_3 = 2.39 \pm 0.07$. The lower boundary of self-similarity of surface-fractal agglomerates of a given structural level is determined by the characteristic size R_{c2} of mass-fractal aggregates of the second structural level. An estimate of the upper limit of the self-similarity of surface-fractal agglomerates of the third structural level can be obtained from the analysis of scattering in the Guinier regime in the range $0.002 < q$ nm^{-1}: $R_{c3} = \left[(D_{s3} + 2)/D_{s3}\right]^{1/2} \cdot R_{g3}$.

Thus, the observed pattern of ultra-small-angle and small-angle neutron scattering by the synthesized TiO$_2$ (No. 8) indicates three types of scattering inhomogeneities in it, which

are different in characteristic scale. It is most likely that this powder consists of large-scale agglomerates with a fractal interface, built of mass-fractal aggregates, which, in turn, consist of mass-fractal clusters. For a general analysis of the observed scattering pattern, a unified exponential-power expression was used, where the presence of several structural levels in the scattering system is taken into account [41]:

$$\frac{d\Sigma(q)}{d\Omega} = \sum_{i=1}^{2}(G_i \cdot \exp\left(-\frac{q^2 R_{gi}^2}{3}\right) + B_i \exp\left(-\frac{q^2 R_{g(i-1)}^2}{3}\right)\left[\frac{(erf(qR_{gi}/\sqrt{6}))^3}{q}\right]^{n_i}) + I_{inc} \qquad (1)$$

The sum (1) is determined by the number of structural levels. In general, expression (1) determines the presence of 4 free parameters for each structural level: G_i is Guinier prefactor for the i-th structural level; gyration radius (directly proportional to particle size); B_i – power prefactor; n_i – exponent connected to the particle aggregation type (fractal dimension of the particle aggregates). The I_{inc} parameter is the q-independent constant caused by the incoherent scattering by hydrogen atoms.

The scattering pattern for the commercial TiO$_2$ (65) sample (Fig. 5b) is typical for systems with a disordered structure consisting of randomly oriented non-spherical (anisodiametric) objects, for example, for highly elongated (fibrils) or flattened (lamellas) particles. This correlates with the results obtained by the SEM method (Fig. 3a) for this sample.

To describe scattering in the Guinier region, where the characteristic size Rc determines scattering and the shape of independently scattering inhomogeneities, regardless of their local structure, it is necessary to use the generalized expression [42]:

$$\frac{d\Sigma(q)}{d\Omega} = \frac{G}{q^s} \cdot \exp(-\frac{q^2 R_g^2}{3-s}), \qquad (2)$$

Here, the amplitude G is directly proportional to the product of the number of inhomogeneities in the scattering volume and the square of the average density ρ of the amplitude of neutron scattering on them [43]. Parameter s is determined by the shape of the scattering inhomogeneities. For spherical objects $s = 0$, for one-dimensional particles (fibrils) $s = 1$, for two-dimensional inhomogeneities (lamellas) $s = 2$. The values of the parameter s can be not only integer but also fractional, for example if the scattering inhomogeneities have the shape of an ellipsoid of revolution or the presence of inhomogeneities of various shapes in the sample.

Since non-spherical objects are determined not by one, but by two (radius R and length L in the case of fibrils) or three (thickness T, width W, and length L for lamellas) characteristic values, the corresponding Guinier region will include two or three ranges by the momentum transfer q. It is fully consistent with the observed experimental data for commercial TiO$_2$ (65). As can be seen in Fig. 5b, four ranges can be distinguished on the dependence of the scattering cross-section d$\Sigma(q)$/dΩ: the range corresponding to the Porod regime, where the scattering is determined by the local structure of scattering inhomogeneities and is described by the power-law q^{-n} dependence, and three regions corresponding to the Guinier regimes, where scattering is determined by the characteristic dimensions of non-spherical scattering inhomogeneities.

The value of the exponent n, determined from the slope of the straight-line section of the experimental dependence d$\Sigma(q)$/dΩ in the range $0.1 < q < 1$ nm^{-1}, equals $n = 4.24 \pm 0.04$. The scattering law with $n > 4$ is typical for porous systems with the so-called "diffuse" surface [44]. In this case, the exponent $n = 4 + 2\beta$, where $0 \leq \beta \leq 1$ is the exponent value that characterizes the change of the nuclear density ρ in the surface layer of inhomogeneities [44].

If we assume that the inhomogeneities have a smooth surface, then the nuclear density ρ will depend only on the distance x from a point on the surface. Thus, the nuclear density $\rho(x)$ can be represented as:

$$\begin{aligned} \rho(x) &= 0 & x < 0 \\ \rho(x) &= \rho_0(x/\alpha)^{\beta} & 0 \leq x \leq \alpha \quad (3) \\ \rho(x) &= \rho_0 & x \leq \alpha, \end{aligned}$$

where α is the width of the transition ("diffuse") layer, in which the nuclear density ρ increases, respectively, from zero to ρ_0. The appearance of such a layer is observed for porous systems (xerogels, nanopowders, aerogels), for example, under the high-temperature annealing [45,46] or as a result of diffuse mixing of chemical elements in the surface layer during alloying.

In the range of large momentum transfer $q > 1$ nm^{-1}, the scattering cross-section $d\Sigma(q)/d\Omega$ ceases to depend on q and corresponds to incoherent scattering by inhomogeneities of the size comparable with neutron wavelength λ used in this experiment.

Thus, to analyze the $d\Sigma(q)/d\Omega$ curve for commercial TiO$_2$ (65), we used the generalized empirical Guinier-Porod model [42]:

$$\frac{d\Sigma(q)}{d\Omega} = G_3 \cdot \exp(-\frac{q^2 R_{g3}^2}{3}) \quad \text{при } q < q_3,$$

$$\frac{d\Sigma(q)}{d\Omega} = \frac{G_2}{q^{s_2}} \cdot \exp(-\frac{q^2 R_{g2}^2}{3 - s_2}) \quad \text{при } q_3 < q < q_2,$$

$$\frac{d\Sigma(q)}{d\Omega} = \frac{G_1}{q^{s_1}} \cdot \exp(-\frac{q^2 R_{g1}^2}{3 - s_1}) \quad \text{при } q_2 < q < q_1, \quad (4)$$

$$\frac{d\Sigma(q)}{d\Omega} = \frac{B_1}{q^{n1}} + I_{inc} \text{при } q > q_1.$$

Here, $(3 - s_2)$ and $(3 - s_1)$ are 'dimensionality' parameters; R_{g1}, R_{g2} and R_{g3} are the characteristic sizes of non-spherical scattering inhomogeneities ($R_{g1} < R_{g2} < R_{g3}$). For lamellas with thickness T, width W and length L: $R_{g3} = (L^2/12 + W^2/12 + T^2/12)^{1/2}$, $R_{g2} = (W^2/12 + T^2/12)^{1/2}$ and $R_{g1} = T/12^{1/2}$. G_3, G_2, and G_1 are the Guinier coefficients [38,42]; B_1 is the coefficient depending on the local structure of scattering inhomogeneities [47]; I_{inc} is a constant caused by the incoherent scattering by hydrogen atoms.

Table 2. Parameters of meso- and microstructure for the synthesized TiO$_2$ (*Syn*) powder obtained from the analysis of USANS and SANS data.

Structural level	G_i, cm^{-1}	R_{ci}, nm	$B_i \cdot 10^3$, cm$^{-1}\cdot$nm^{-n}	$D_s = 6 - n_i$	$D_m = n_i$
USANS					
3rd	88600 ± 2200	1940 ± 180	0.004 ± 0.001	2.39 ± 0.07	-
USANS + SANS					
2nd	3140 ± 430	654 ± 46	2.6 ± 0.8	-	2.61 ± 0.04
SANS					
1st	3.4 ± 0.2	14 ± 1	57 ± 2	-	2.23 ± 0.04

Note: G_i – the Guinier coefficient for the i-th structural level; R_{ci} – upper limit of the self-similarity of fractal for the i-th structural level; B_i – power prefactor for the i-th structural level; D_m – mass fractal dimension; D_s – surface fractal dimension.

To obtain final results using expressions (1) and (4), the experimental dependences of the differential scattering cross-section $d\Sigma(q)/d\Omega$ were processed by the least-squares method in the entire range. The results of this analysis are presented in Fig. 5 a, b, and in Tables 2 and 3.

Complex analysis (SEM, USANS, SANS data, and low-temperature nitrogen adsorption) shows that the commercial TiO$_2$ (*Com*) powder is formed by weakly porous large-scale aggregates ($S_{Langmuir} \approx 6$ m^2/g) with an anisodiametric shape close to a parallelepiped, with a thickness of $T \approx 30$ nm, a width of $W \approx 160$ nm, and a length of $L \approx 1$ µm, respectively, possessing a "diffuse" surface.

Table 3. Parameters of meso- and microstructure for commercial TiO$_2$ (*Com*) powder obtained from the analysis of USANS and SANS data.

G_i, cm^{-1}	s_i	R_{gi}, nm	$B \cdot 10^3$, cm$^{-1} \cdot$nm^{-n}	$n = 4 + 2\beta$
Low-q Guinier region				
817500 ± 25000	0	790 ± 50	-	-
Intermadiate-q Guinier region				
13.3 ± 2.3	1.61 ± 0.03	46.3 ± 5.7	-	-
High-q Guinier region				
1.3 ± 0.1	2.10 ± 0.02	8.1 ± 0.3	-	-
Porod region				
-	-	-	4.6 ± 0.2	4.24 ± 0.04

Note: G_i – the Guinier coefficients; s_i – 'dimensionality' parameters; R_{gi} – the characteristic sizes of non-spherical scattering inhomogeneities; B – the coefficient depending on the local structure of scattering inhomogeneities; n – the exponent.

The synthesized TiO$_2$ (*Syn*) powder has a highly porous ($S_{BET} \approx 370$ m^2/g) three-level hierarchical structure. At the first structural level, the structure is made of mass-fractal clusters with a dimension $Dm = 2.35 \pm 0.04$ and a characteristic size (along the upper self-similarity boundary) $R_{c1} \approx 14$ nm. These clusters at the second structural level form the denser mass-fractal aggregates with a dimension $D_m = 2.61 \pm 0.04$ and a characteristic size (along with the upper self-similarity limit) $R_{c2} \approx 150$ nm. They, in turn, at the third structural level form large-scale agglomerates with a fractal surface (solid-phase - pore) with a dimension $Ds = 2.39 \pm 0.07$ and a characteristic size (along the upper self-similarity boundary) $R_{c3} \approx 1.9$ µm.

3.2. Photocatalytic activity of TiO$_2$ powders.

The study of the titanium dioxide powders' photocatalytic activity showed that the highest and most stable activity is possessed by a well-crystallized commercial TiO$_2$ (*Com*) powder. After 6 days of exposure of this sample to UV radiation, the singlet oxygen release activity was 20 times higher than synthesized TiO$_2$ (Syn) powder. The data obtained can be explained by the presence of well-crystallized TiO$_2$ phases in the sample with more active photocatalytic properties. The synthesized TiO$_2$ nanopowder (Syn) that has not undergone high-temperature treatment is poorly crystallized.

3.3 Biological activity of the studied TiO$_2$ nanopowders.

Table 4 presents the data regarding the effect of pre-sowing treatment of white cabbage (Penca de Povoa) seeds with aqueous suspensions of the studied TiO$_2$ powders on the germination energy, germination, and biometric parameters of their seedling's growth.

Treatment of seeds with titanium dioxide suspensions has an ambiguous effect on their germination energy and germination capacity.

Analysis of the data indicates that in all variants of processing white cabbage seeds with the TiO$_2$ suspensions, there is significant stimulation of the sprouts' growth (by 23-36%) and roots growth (by 13-55%), while there is no significant difference in terms of germination energy and germination plant seeds in comparison with the control. It should be noted of a tendency that the germination rate exceeds the control values in the variants of seed treatment with suspensions of 0.3 g/l of synthesized TiO$_2$ (Syn) (by 13%) or 0.3 g/l of commercial TiO$_2$ (Com) (by 8%). With an increase in titanium dioxide powders' concentration up to 3 g/l, no tendency to stimulate seed germination is observed.

Table 4. Biological activity of the TiO$_2$ suspensions towards white cabbage variety Penca de Povoa seeds.

Suspension	Germination energy		Germination		Sprout length		Root length	
	%	% of control	%	% of control	cm	% of control	cm	% of control
Water + 0 g/l TiO$_2$ (control)	84	100	80	100	2,2±0,2	100	4,0±0,4	100
Water + 0,3 g/l TiO$_2$ (Com)	75	89	86	108	2,7±0,2*	123*	5,3±0,5*	133*
Water + 3 g/l TiO$_2$ (Com)	75	89	78	98	2,8±0,2*	127*	5,2±0,4*	130*
Water + 0,3 g/l TiO$_2$ (Syn)	88	105	90	113	3,0±0,2*	136*	6,2±0,5*	155*
Water + 3 g/l TiO$_2$ (Syn)	80	95	77	96	2,9±0,2*	132*	4,5±0,4	113

Note: * - the value significantly differs from the control at a 5% significance level.

The highest values of growth for both roots and sprouts of white cabbage variety Penca de Povoa were detected in the variant of seed treatment with a suspension with 0.3 g/l of synthesized TiO$_2$ (Syn). An increase in the concentration of the TiO$_2$ (Syn) suspensions up to 3 g/l mainly leads to a decrease in the stimulating effect.

Thus, the synthesized TiO$_2$ (*Syn*) powder has a better biological activity regarding the seeds of white cabbage (Penca de Povoa) in comparison with commercial TiO$_2$ (*Com*). Such a result can be explained by the fact that the synthesized titanium dioxide TiO$_2$ (*Syn*) has an amorphous structure and consists of inhomogeneities 10-20 nm in size, and therefore it can be dispersed in water evenly, partially dissolving. This, in turn, contributes to the distribution of TiO$_2$ not only over the surface of the seeds but also provides penetration deeper into the surface layer. The influence of photocatalytic activity on the studied parameters of seeds is not explicitly observed. It may have manifested itself in a decrease in parameters, especially the germination energy of seeds treated in suspensions with commercial TiO$_2$ (*Com*), although this may also be related to the effect of a large amount of rutile phase in this powder. Further research is needed for a solid conclusion.

4. Conclusions

TiO$_2$ nanopowder has been prepared with aqueous chemical synthesis for use in agriculture. A commercial nanopowder was taken for comparison. A comprehensive study of the phase composition, morphology, and structure of titanium dioxide powders was carried out

using XRD, Raman spectroscopy, SEM, low-temperature nitrogen adsorption, and SANS methods. It was found that the commercial TiO_2 powder produced by Plasmotherm® (Russia) is a mixture of anatase and rutile in the weight ratio of 1:4, in the form of weakly porous large-scale aggregates ($S_{Langmuir} \approx 6$ m^2/g) with an anisodiametric shape close to a parallelepiped with a thickness 30 nm, a width 160 nm, and a length 1 µm, respectively, possessing a "diffuse" surface.

The synthesized TiO_2 powder has a highly porous ($S_{BET} \approx 370$ m^2/g) three-level hierarchical structure. At the first structural level, the structure is made of mass-fractal clusters with a characteristic size (along the upper self-similarity boundary) $R_c \approx 14$ nm. At the second structural level, these clusters form the denser mass-fractal aggregates with a characteristic size (along with the upper self-similarity limit) $R_c \approx 150$ nm. They, in turn, at the third structural level form large-scale agglomerates with a fractal surface (solid-phase - pore) with a characteristic size (along the upper self-similarity boundary) $R_c \approx 1.9$ µm.

In terms of the amount of singlet oxygen released under the action of UV radiation, the photocatalytic activity of well-crystallized commercial TiO_2 (anatase/rutile = 1/4) is 20 times higher than that of poorly crystallized anatase synthesized by precipitation from an aqueous solution.

A direct correlation was revealed between the structure and biological activity of the studied TiO_2 nanopowders regarding the seeds of white cabbage (Penca de Povoa). It was found that the synthesized TiO_2 used for pre-sowing seed treatment in the form of an aqueous suspension with a concentration of 0.3 g/l showed higher biological activity, which manifested itself in a significant or in the form of a tendency to stimulate the germination and biometric characteristics of plants' growth at the early stages of their development. An increase in the concentration of titanium dioxide powders to 3 g/l generally leads to a decrease in seeds' studied characteristics. At the same time, no direct correlation between the photocatalytic and biological activity of TiO_2 with respect to seeds was revealed in this study; this requires additional research.

Funding

Acknowledgments

Conflicts of Interest

The authors declare no conflict of interest.

References

1. Chaudhary, I.J.; Singh, V. Titanium dioxide nanoparticles and its impact on growth, biomass and yield of agricultural crops under environmental stress: A review. *Research Journal of Nanoscience and Nanotechnology* **2020**, *10*, 1-8, https://doi.org/10.3923/rjnn.2020.1.8.

2. Paramo, L.A.; Feregrino-Pérez, A.A.; Guevara, R.; Mendoza, S.; Esquivel, K. Nanoparticles in Agroindustry: Applications, Toxicity, Challenges, and Trends. *Nanomaterials* **2020**, *10*, 1654, https://doi.org/10.3390/nano10091654.

3. Shang, Y.; Hasan, M.; Ahammed, G.J.; Li, M.; Yin, H.; Zhou, J. Applications of nanotechnology in plant growth and crop protection: a review. *Molecules* **2019**, *24*, 2558, https://doi.org/10.3390/molecules24142558.

4. Usman, M.; Farooq, M.; Wakeel, A.; Nawaz, A.; Cheema, S.A.; Rehman, H.u.; Ashraf, I.; Sanaullah, M. Nanotechnology in agriculture: Current status, challenges and future opportunities. *Sci. Total Environ.* **2020**, *721*, 137778, https://doi.org/10.1016/j.scitotenv.2020.137778.

5. Acharya, P.; Jayaprakasha, G.K.; Crosby, K.M.; Jifon, J.L.; Patil, B.S. Nanoparticle-Mediated Seed Priming Improves Germination, Growth, Yield, and Quality of Watermelons (Citrullus lanatus) at multi-locations in Texas. *Sci. Rep.* **2020**, *10*, 5037, https://doi.org/10.1038/s41598-020-61696-7.

6. Bellani, L.; Siracusa, G.; Giorgetti, L.; Di Gregorio, S.; Ruffini Castiglione, M.; Spanò, C.; Muccifora, S.; Bottega, S.; Pini, R.; Tassi, E. TiO2 nanoparticles in a biosolid-amended soil and their implication in soil nutrients, microorganisms and Pisum sativum nutrition. *Ecotoxicol. Environ. Saf.* **2020**, *190*, 110095, https://doi.org/10.1016/j.ecoenv.2019.110095.

7. Wu, X.; Hu, J.; Wu, F.; Zhang, X.; Wang, B.; Yang, Y.; Shen, G.; Liu, J.; Tao, S.; Wang, X. Application of TiO2 nanoparticles to reduce bioaccumulation of arsenic in rice seedlings (Oryza sativa L.): A mechanistic study. *J. Hazard. Mater.* **2020**, 124047, https://doi.org/10.1016/j.jhazmat.2020.124047.

8. Ullah, S.; Adeel, M.; Zain, M.; Rizwan, M.; Irshad, M.K.; Jilani, G.; Hameed, A.; Khan, A.; Arshad, M.; Raza, A.; Baluch, M.A.; Rui, Y. Physiological and biochemical response of wheat (Triticum aestivum) to TiO2 nanoparticles in phosphorous amended soil: A full life cycle study. *J. Environ. Manage.* **2020**, *263*, 110365, https://doi.org/10.1016/j.jenvman.2020.110365.

9. Lian, J.; Zhao, L.; Wu, J.; Xiong, H.; Bao, Y.; Zeb, A.; Tang, J.; Liu, W. Foliar spray of TiO2 nanoparticles prevails over root application in reducing Cd accumulation and mitigating Cd-induced phytotoxicity in maize (Zea mays L.). *Chemosphere* **2020**, *239*, 124794, https://doi.org/10.1016/j.chemosphere.2019.124794.

10. Sun, D.; Hussain, H.I.; Yi, Z.; Rookes, J.E.; Kong, L.; Cahill, D.M. Mesoporous silica nanoparticles enhance seedling growth and photosynthesis in wheat and lupin. *Chemosphere* **2016**, *152*, 81-91, https://doi.org/10.1016/j.chemosphere.2016.02.096.

11. Singh R.P., Handa R., Manchanda G. Nanoparticles in sustainable agriculture: An emerging opportunity, *Journal of Controlled Release* **2020**, https://doi.org/10.1016/j.jconrel.2020.10.051.

12. Pariona, N.; Martínez, A.I.; Hernandez-Flores, H.; Clark-Tapia, R. Effect of magnetite nanoparticles on the germination and early growth of Quercus macdougallii. *Sci. Total Environ.* **2017**, *575*, 869-875, https://doi.org/10.1016/j.scitotenv.2016.09.128.

13. Li, J.; Hu, J.; Ma, C.; Wang, Y.; Wu, C.; Huang, J.; Xing, B. Uptake, translocation and physiological effects of magnetic iron oxide (γ-Fe2O3) nanoparticles in corn (Zea mays L.). *Chemosphere* **2016**, *159*, 326-334, https://doi.org/10.1016/j.chemosphere.2016.05.083.

14. Feizi, H.; Rezvani Moghaddam, P.; Shahtahmassebi, N.; Fotovat, A. Impact of Bulk and Nanosized Titanium Dioxide (TiO2) on Wheat Seed Germination and Seedling Growth. *Biol. Trace Elem. Res.* **2012**, *146*, 101-106, https://doi.org/10.1007/s12011-011-9222-7.

15. Siddiqui M.H., Al-Whaibi M.H., Firoz M., Al-Khaishany M.Y. (2015) Role of Nanoparticles in Plants. In: Siddiqui M., Al-Whaibi M., Mohammad F. (eds) Nanotechnology and Plant Sciences. Springer, Cham. https://doi.org/10.1007/978-3-319-14502-0_2.

16. Astafurova, T.P.; Morgalev, Y.N.; Zotikova, A.P.; Verkhoturova, G.S.; Mikhajlova, S.I.; Burenina, A.A.; Zajtseva, T.A.; Postovalova, V.M.; Tsytsareva, L.K.; Borovikova, G.V. Effect of nanoparticles of titanium dioxide and aluminum oxide on some morphophysiological characteristics of plants. *Bulletin of Tomsk State University. Biology* **2011.**

17. Silva, S.; Oliveira, H.; Silva, A.M.S.; Santos, C. The cytotoxic targets of anatase or rutile + anatase nanoparticles depend on the plant species. *Biol. Plant.* **2017**, *61*, 717-725, https://doi.org/10.1007/s10535-017-0733-8.

18. Rizwan, M., Ali, S., ur Rehman, M.Z. et al. Effect of foliar applications of silicon and titanium dioxide nanoparticles on growth, oxidative stress, and cadmium accumulation by rice (Oryza sativa). *Acta Physiol Plant* **2019,** *41*, 35. https://doi.org/10.1007/s11738-019-2828-7.

19. Tekin, D.; Birhan, D.; Kiziltas, H. Thermal, photocatalytic, and antibacterial properties of calcinated nano-TiO2/polymer composites. *Mater. Chem. Phys.* **2020**, *251*, 123067, https://doi.org/10.1016/j.matchemphys.2020.123067.

20. Sakurai, H.; Kiuchi, M.; Jin, T. Macroaggregation effect of TiO2 nanoparticles on the photocatalytic activity and post-reaction separation for aqueous degradation of organic compounds. *Journal of Environmental Chemical Engineering* **2020**, 104936, https://doi.org/10.1016/j.jece.2020.104936.

21. Shilova, O.A.; Khamova, T.V.; Panova, G.G.; Kornyukhin, D.L.; Anikina, L.M.; Artemyeva, A.M.; Udalova, O.R.; Galushko, A.S.; Baranchikov, A.E. Synthesis and Research of Functional Layers Based on Titanium Dioxide Nanoparticles and Silica Sols Formed on the Surface of Seeds of Chinese Cabbage. *Russ. J. Appl. Chem.* **2020**, *93*, 25-34, https://doi.org/10.1134/S1070427220010036.

22. Gregg, S.J.; Sing, K.S.W. Adsorption, surface area and porosity. Academic Press, London. *Adsorption, surface area and porosity. 2nd ed. Academic Press, London.* **1982.**

23. Kuklin, A.I.; Islamov, A.K.; Gordeliy, V.I. Scientific Reviews: Two-Detector System for Small-Angle Neutron Scattering Instrument. *Neutron News* **2005**, *16*, 16-18, https://doi.org/10.1080/10448630500454361.

24. Soloviev, A.G.; Solovieva, T.M.; Stadnik, A.V.; Islamov, A.H.; Kuklin, A.I. The package for small-angle neutron scattering data treatment. *JINR Commun* **2003**, *10*, 2003-2086.

25. Ostanevich, Y.M. Time-of-flight small-angle scattering spectrometers on pulsed neutron sources. *Makromolekulare Chemie. Macromolecular Symposia* **1988**, *15*, 91-103, https://doi.org/10.1002/masy.19880150107.

26. Radulescu, A.; Kentzinger, E.; Stellbrink, J.; Dohmen, L.; Alefeld, B.; Rücker, U.; Heiderich, M.; Schwahn, D.; Brückel, T.; Richter, D. KWS-3: The New (Very) Small-Angle Neutron Scattering Instrument Based on Focusing-Mirror Optics. *Neutron News* **2005**, *16*, 18-21, https://doi.org/10.1080/10448630500454270.

27. Goerigk, G.; Varga, Z. Comprehensive upgrade of the high-resolution small-angle neutron scattering instrument KWS-3 at FRM II. *J. Appl. Crystallogr.* **2011**, *44*, 337-342, https://doi.org/10.1107/S0021889811000628.

28. Wignall, G.T.; Bates, F.S. Absolute calibration of small-angle neutron scattering data. *J. Appl. Crystallogr.* **1987**, *20*, 28-40, https://doi.org/10.1107/S0021889887087181.

29. Jülich Centre for Neutron Science, QtiKWS 2019. Available online: www.qtisas.com

30. Chelibanov, V.P.; Chelibanov, I.V.; Frank-Kamenetskaya, O.V.; Iasenko, E.A.; Marugin, A.M.; Pinchuk, O.A. Singlet Oxygen in the Lower Atmosphere: Origin, Measurement and Participation in Processes and Phenomena at the Boundary Between Biogenic and Abiogenic Nature. In *Processes and Phenomena on the Boundary Between Biogenic and Abiogenic Nature*, Springer: 2020; 137-153.

31. Daimon, T.; Nosaka, Y. Formation and Behavior of Singlet Molecular Oxygen in TiO2 Photocatalysis Studied by Detection of Near-Infrared Phosphorescence. *The Journal of Physical Chemistry C* **2007**, *111*, 4420-442, https://doi.org/10.1021/jp070028y.

32. International Rules for Seed Testing, Volume 2020, Number 1, January 2020, pp. i-19-8(8) https://doi.org/10.15258/istarules.2020.F.

33. Beaucage, G.; Ulibarri, T.A.; Black, E.P.; Schaefer, D.W. Multiple Size Scale Structures in Silica—Siloxane Composites Studied by Small-Angle Scattering. In *Hybrid Organic-Inorganic Composites*, American Chemical Society: 1995; Vol. 585, 97-111.

34. Štěpánek, M.; Matějíček, P.; Procházka, K.; Filippov, S.K.; Angelov, B.; Šlouf, M.; Mountrichas, G.; Pispas, S. Polyelectrolyte−Surfactant Complexes Formed by Poly[3,5-bis(trimethylammoniummethyl)4-hydroxystyrene iodide]-block-poly(ethylene oxide) and Sodium Dodecyl Sulfate in Aqueous Solutions. *Langmuir* **2011**, *27*, 5275-5281, https://doi.org/10.1021/la200442s.

35. Gubanova, N.N.; Kopitsa, G.P.; Ezdakova, K.V.; Baranchikov, A.E.; Angelov, B.; Feoktystov, A.; Pipich, V.; Ryukhtin, V.; Ivanov, V.K. Structure of Porous Glasses Based on Zirconium Dioxide. *Journal of Surface Investigation. Xray, Synchrotron and Neutron Techniques*, **2014**, *8*, 967–975, https://doi.org/10.7868/S0207352814100072.

36. Khamova, T.V.; Shilova, O.A.; Kopitsa, G.P.; Angelov, B.; Zhigunov, A. Effect of biocidal additives on the mesostructure of epoxy–siloxane bioactive coatings. *Journal of Surface Investigation. X-ray, Synchrotron and Neutron Techniques* **2016**, *10*, 113-122, https://doi.org/10.7868/S0207352815120094.

37. Teixeira, J. Experimental methods for studying fractal aggregates. In *On growth and form*, Springer: 1986; 145-162.

38. Guinier, A.; Fournet, G.; Yudowitch, K.L. Small-angle scattering of X-rays. **1955**.

39. Oh, C.; Sorensen, C.M. The Effect of Overlap between Monomers on the Determination of Fractal Cluster Morphology. *J. Colloid Interface Sci.* **1997**, *193*, 17-25, https://doi.org/10.1006/jcis.1997.5046.

40. Bale, H.D.; Schmidt, P.W. Small-Angle X-Ray-Scattering Investigation of Submicroscopic Porosity with Fractal Properties. *Phys. Rev. Lett.* **1984**, *53*, 596-599, https://doi.org/10.1103/PhysRevLett.53.596.

41. Beaucage, G. Approximations leading to a unified exponential/power-law approach to small-angle scattering. *J. Appl. Crystallogr.* **1995**, *28*, 717-728, https://doi.org/10.1107/s0021889895005292.

42. Hammouda, B. A new Guinier–Porod model. *J. Appl. Crystallogr.* **2010**, *43*, 716-719, https://doi.org/10.1107/S0021889810015773.

43. Glatter, O.; Kratky, O. *Small angle X-ray scattering*; Academic press: 1982.

44. Schmidt, P.W.; Avnir, D.; Levy, D.; Höhr, A.; Steiner, M.; Röll, A. Small-angle x-ray scattering from the surfaces of reversed-phase silicas: Power-law scattering exponents of magnitudes greater than four. *The Journal of Chemical Physics* **1991**, *94*, 1474-1479, https://doi.org/10.1063/1.460006.

45. Ivanov, V.K.; Maksimov, V.D.; Shaporev, A.S.; Baranchikov, A.E.; Churagulov, B.P.; Zvereva, I.A.; Tret'yakov, Y.D. Hydrothermal synthesis of efficient TiO2-based photocatalysts. *Russian Journal of Inorganic Chemistry* **2010**, *55*, 150-154, https://doi.org/10.1134/S0036023610020026.

46. Azarova, L.A.; Kopitsa, G.P.; Iashina, E.G.; Garamus, V.M.; Grigoriev, S.V. Model of Fractal Particles of Hydrated Zirconium Dioxide, Based on Small-Angle Neutron Scattering Data. *Journal of Surface Investigation: X-ray, Synchrotron and Neutron Techniques* **2019**, *13*, 908-913, https://doi.org/10.1134/s0207352819100044.

47. Schmidt, P.W. Some fundamental concepts and techniques useful in small-angle scattering studies of disordered solids. In *Modern aspects of small-angle scattering*, Springer: 1995; 1-56.